RSC Advances

PAPER

View Article Online
View Journal | View Issue

Cite this: *RSC Adv.*, 2019, **9**, 7723

Improving gas sensing performance by oxygen vacancies in sub-stoichiometric WO_{3-x}

Weiwei Yu,[ab] Zhenguang Shen,[c] Fang Peng,[ab] Yue Lu,[a] Meiying Ge,[d] Xiuli Fu,[c] Yan Sun,*[a] Xin Chen*[a] and Ning Dai*[a]

Received 6th January 2019
Accepted 23rd February 2019

DOI: 10.1039/c9ra00116f

rsc.li/rsc-advances

Sub-stoichiometric WO_{3-x} has provided an alternative platform to investigate oxygen vacancies in gas sensors based on metal-oxides. We present an experimental study on the influence of sub-stoichiometric WO_{3-x} phase upon gas sensing performance. High-quality WO_{3-x} nanostructures with several x values (WO_3, $W_{19}O_{55}$, W_5O_{14}, $W_{18}O_{49}$) were synthesized and used to fabricate H_2S gas sensors. Temperature programmed desorption of oxygen (O_2-TPD) shows that oxygen absorption behaviors of the as-prepared WO_{3-x} nanostructures are affected by oxygen vacancies, which played a critical role in the detection of H_2S at varying temperature range. We find that oxygen vacancies in sub-stoichiometric WO_{3-x} facilitate the ionosorption process and in turn enhance the performance of the gas sensor.

Introduction

According to the "ionosorption model", ionosorbed oxygen species (*i.e.* O_2^-, O^-, O^{2-}) on semiconductor surfaces determine the gas sensing behavior.[1–3] So far, considerable efforts have been applied to facilitate the oxygen ionosorption for enhancing the gas sensing performance and various strategies are adopted to manipulate oxygen absorption, such as changing morphologies,[4–6] changing sizes and dimensions of micro or nano materials,[7–9] and using catalysts[10,11] or UV-light irradiation.[12,13] Recently, oxygen vacancies have been found to play a critical role in influencing the gas sensing process and determining the performance of gas sensors. For example, density functional theory (DFT) has been successfully employed to study the effect of oxygen deficiency on the electronic and structural properties of sub-stoichiometric tungsten oxides (WO_{3-x}).[14–17] F. Wang, *et al.*, reported the computational results that revealed the strong dependence of WO_{3-x} electronic properties on oxygen vacancies.[15] J. Song, *et al.*, simulated the kinetic and thermodynamic processes of H_2 adsorption, activation, and dissociation on $WO_{2.72}$ surface.[16] High sensitive NO_2 gas sensors based on $W_{18}O_{49}$ nanowires have been fabricated and the improvement of the sensing performance are due to oxygen vacancies in $W_{18}O_{49}$.[18] Monoclinic $W_{18}O_{49}$ is a well-studied sub-stoichiometric phase and can easily be isolated in a pure form.[19–21] In fact, sub-stoichiometric WO_{3-x} materials have provided a powerful platform to investigate the gas sensing behaviour associated with oxygen vacancies in metal-oxides based gas sensors. However, it is a challenging task to control oxygen vacancies in sub-stoichiometric WO_{3-x} accurately.

In this work, we synthesised several sub-stoichiometric WO_{3-x}, including $W_{19}O_{55}$, W_5O_{14} and $W_{18}O_{49}$, and fabricated gas sensors using the materials. We systematically studied the role of oxygen vacancies in sensing properties of the gas sensors. It was found that oxygen vacancies affected oxygen absorption on the surface of the WO_{3-x} nanostructures, and facilitated the ionosorption process, favourable for improving device performance and lowering operating temperature. Manipulation of oxygen vacancies in metal oxides brings us an alternative way to improve the performance of gas sensing devices.

Experimental

Synthesis of tungsten oxide samples

WO_3 powder was synthesized in a typical hydrothermal method as we had reported before.[22] The sub-stoichiometric tungsten oxides (*e.g.* $W_{19}O_{55}$, W_5O_{14}, $W_{18}O_{49}$) were obtained by the reduction of WO_3 powders with S powders. The chemical compositions in the sub-stoichiometric tungsten oxides were controlled by the growth temperature. In the growth system, the as-prepared WO_3 powder was located in the middle of a vacuum tube furnace, while S powder was deposited at its upstream position. After evacuating pre-treatment and repeating flush with pure Ar gas, the tube furnace was heated up to the target temperature and dwelled for one hour.[23] The raw WO_3 powders were then annealed at 500 °C in atmospheric environment. $W_{19}O_{55}$ (dark-blue), W_5O_{14} (purple-blue), and $W_{18}O_{49}$ (purple-

[a]State Key Laboratory of Infrared Physics, Shanghai Institute of Technical Physics, Chinese Academy of Sciences, Shanghai 200083, China. E-mail: xinchen@mail.sitp.ac.cn; ndai@mail.sitp.ac.cn

[b]University of Chinese Academy of Sciences, Beijing 100049, China

[c]School of Science, Beijing University of Posts and Telecommunications, Beijing 100876, China

[d]National Engineering Research Center for Nanotechnology, No. 28 East Jiang Chuan Road, Shanghai 200241, China

red) were synthesized at 950, 1050, 1150 °C in the vacuum tube furnace, respectively. The corresponding colours of the resulting sub-stoichiometric tungsten oxides depend on their chemical compositions, as reported in literatures.[19,24–26]

Sample characterization and gas sensors measurements

The morphologies of the obtained sub-stoichiometric nanomaterials were examined by a field emission scanning electron microscope (SEM, FEI Sirion 200). Transmission electron microscopy (TEM) and high-resolution transmission electron microscopy (HRTEM, JEOL2100F transmission electron microscope) was adopted to study the crystallographic structures. The phase and composition were investigated by X-ray diffractometry (XRD, Bruker D8 Avance) with a Cu Kα radiation source (40 kV and 40 mA). X-ray photoelectron spectrometer (XPS, ESCALAB 250Xi, Thermo Scientific) was employed to identify the elements and chemical states by using sub-monochromatized Al KR X-ray as the excitation source. The spectrometer was calibrated with the binding energy of the C 1s line (284.5 eV). Gas sensing test was performed on the HW-30A system (Hanwei Electronics Co. Ltd., PR China).

Results and discussions

Morphology, structure and composition characterization

The XRD results of the as-prepared WO_3, $W_{19}O_{55}$, W_5O_{14}, and $W_{18}O_{49}$ are present in Fig. 1. Fig. 2 illustrates the SEM and HRTEM images of the samples. Grown at different temperatures, the pristine WO_3 crystal exhibits irregular rod-like shape as shown in Fig. 2(a) and the $W_{19}O_{55}$, W_5O_{14}, and $W_{18}O_{49}$ samples show the similar micro and nano rod shapes with flat and smooth surface. The crystal nucleus grows promptly along the preferential growth direction, leading to such symmetric structures. The sub-stoichiometric $W_{19}O_{55}$, W_5O_{14}, and $W_{18}O_{49}$ are well crystalline with clear grain boundaries and ordered crystal planes as shown in Fig. 2(b–d). The diffraction curve recorded in Fig. 1(a) (black line) can be well indexed to the phase of monoclinic WO_3 (JCPDS no. 43-1035), with three main diffraction peaks located at $2\theta = 23.12$, 23.59, and 24.38°, corresponding to the preferential growth directions of [002], [020], [200], respectively. The (002) plane with d-spacing of 3.84 Å is further demonstrated by the HRTEM image in Fig. 2(e).[27] The blue curve in Fig. 1(b) matches well with $W_{19}O_{55}$ (JCPDS no. 45-0167) and the strongest diffraction peak located at $2\theta = 23.47°$ corresponds to the (010) facet with an interlayer distance of 3.7 Å as shown in Fig. 2(f).[28] The diffraction peaks of the red curve in Fig. 1(c) are in good agreement with JCPDS no. 71-0292 file for W_5O_{14}. The main peak located at $2\theta = 23.41°$ suggests the (001) planes with interlayer distance of 3.797 Å, which is a close match to the HRTEM result of 3.79 Å in Fig. 2(g). The W_5O_{14} sample grown in a longitudinal direction along the (001) crystallographic axis has the high aspect ratio of nanorods as shown in the SEM image.[24] At last, Fig. 1(d) depicts the XRD curve of monoclinic $W_{18}O_{49}$ (JCPDS no. 05-0392) with the main peak located at 23.45° corresponding to (010) planes, and the

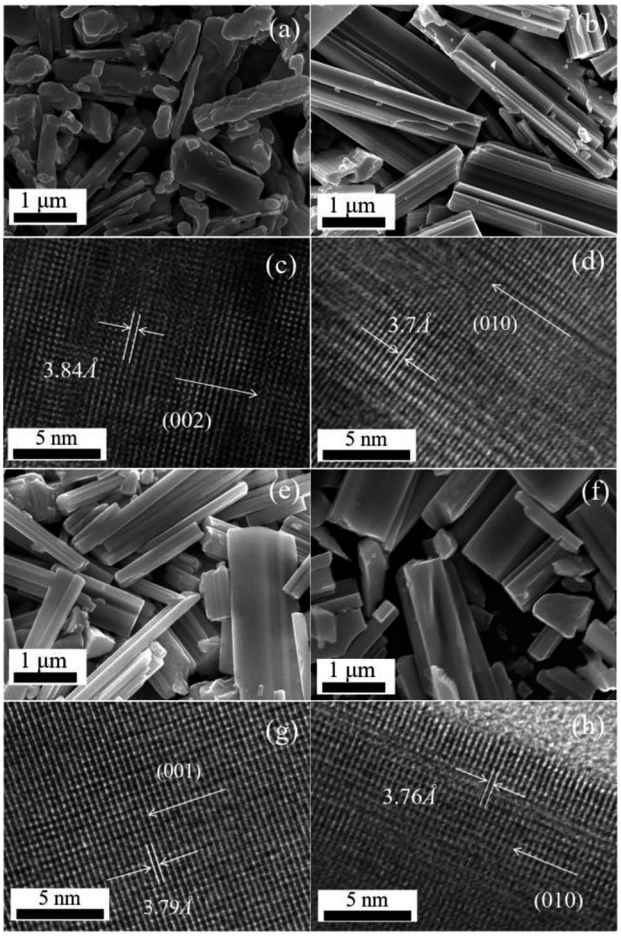

Fig. 2 SEM morphologies and HRTEM images of WO_3 (a and c), $W_{19}O_{55}$ (b and d), W_5O_{14} (e and g), $W_{18}O_{49}$ (f and h).

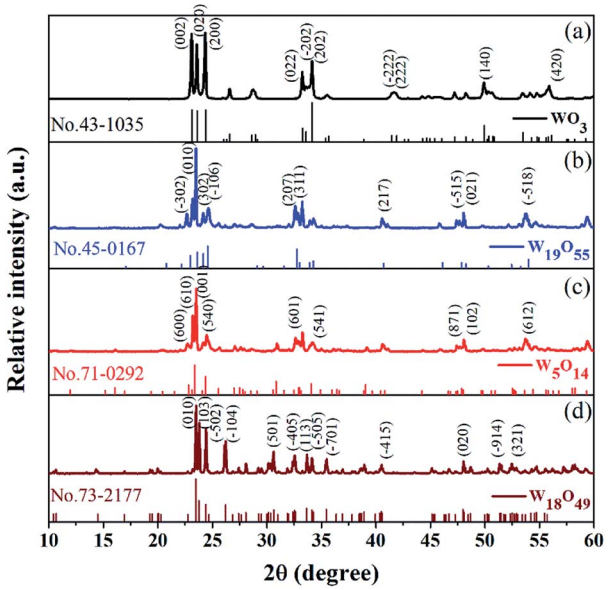

Fig. 1 XRD curves of the as-prepared WO_3 and sub-stoichiometric WO_{3-x}, with standard JCPDS card marked below the corresponding curves.

interlayer distance of 3.8 Å is consistent with the HRTEM value, 3.76 Å, as depicted in Fig. 2(h).[18,19,29]

X-ray photoelectron spectroscopy (XPS) provides an appropriate solution to investigate the chemical composition and element states. As we know, tungsten has a complex distribution of W 4f binding energies consisted of three pairs of doublets (six peaks). As exhibited in Fig. 3(a–d), the thin black line is raw data and the red one is the result of smooth fitting. The first doublet peaks (blue line) locate at 37.85 eV and 35.75 eV corresponding to W $4f_{5/2}$ and W $4f_{7/2}$, which confirms that the W ions are dominated by W^{6+} in WO_3. No W^{5+} and W^{4+} peaks are observed in Fig. 3(a). However, on the other three samples synthesized at 950, 1050, 1150 °C, we observe the mixture of W^{6+}, W^{5+} and W^{4+} oxidation states. As revealed in Fig. 3(b), the second doublet peaks (green dot-curve) appearing at 36.85 and 33.85 eV are attributed to the W^{5+} state. The third doublet peaks occur at 35.25 and 32.5 eV (see the navy dot line), implying the presence of the W^{4+} oxidation state.[26] Thus, as shown by Fig. 3, the contents of W^{5+} and W^{4+} tend to increase gradually with increasing growth temperature. Moreover, we have concluded the O 1s-level XPS spectra of the four WO_{3-x} samples in Fig. 3(e–h), the thin black line is raw data and the red one is the sum of four deconvolution spectra. The first peak (blue line) locate at 530.9 eV corresponding to oxygen atoms O^{2-} in the lattice, and the second peak (green line) locate at 532 eV corresponding to adsorbed oxygen species and oxygen state O^{1-}.[30,31] Metal oxide surfaces that are exposed to the atmosphere are always hydrated, so that hydroxyl groups (–OH) and water molecules (H_2O) signals are also found at 531.4, 532.8 eV, respectively.[31] Our XPS results are in perfect agreement with the report by A. P. Shpak in 2007.[31]

As we can see in Fig. 3(e), oxygen states of O^{2-} are dominated in WO_3 sample, the content of O^{1-} or remnants of adsorbed oxygen species are much smaller than that of O^{2-} state. However, the intensity ratio of O^{2-}/O^{1-} is increasing continuously from WO_3 to $W_{18}O_{49}$, which further confirms the enhanced oxygen adsorption performance in the sub-stoichiometric tungsten oxide. This is the main reason why sensing performance is improved in WO_{3-x} samples. However, the adsorption of H_2O molecules in atmosphere and the formation of –OH groups are also enhanced in the non-stoichiometric WO_{3-x}, which is supposed to suppress the sensing process. This explains why our sensing response of WO_{3-x} samples are improved but with a limited improvement.

From the Raman curves in Fig. 4, Raman characteristic peaks of WO_3 are very clearly exhibited at 806 cm^{-1}, 716 cm^{-1}, 326 cm^{-1} and 272 cm^{-1}.[28,31] However, much wider peaks are observed at 300 and 800 cm^{-1} on the sub-stoichiometric tungsten oxide samples. Due to the distortions in the crystalline structure, it is difficult to assign each of the bands to certain vibrations, particularly for the bands below 300 cm^{-1} which might be deconvoluted into several deformation and lattice vibrations. As exhibited in Fig. 4(b–d), the main bands of $W_{19}O_{55}$, W_5O_{14}, and $W_{18}O_{49}$ are located at 816 cm^{-1}, 805 cm^{-1} and 801 cm^{-1}, respectively. The main band shifts to lower wave number (lower energy) with increasing x value, indicating that more content of reduced tungsten state (W^{4+}, W^{5+}) were formed in the sub-stoichiometric phases.[28,29,32]

Gas sensing properties and discussion

The as-grown sub-stoichiometric tungsten oxides have stable chemical properties and have become an alternative platform to investigate the behaviour of oxygen vacancies in metal-oxides based gas sensors.[23] Fig. 5 shows temperature-dependent sensitivity curves of WO_3 (a), $W_{19}O_{55}$ (b), W_5O_{14} (c), and $W_{18}O_{49}$ (d) when the sensors are exposed to different concentrations of H_2S (1, 2, 3, 4, 10, 50 ppm), marked in different shades of colours. Firstly, it is found that the low-temperature performance of the sub-stoichiometric WO_{3-x} sensors has a tendency to improve as the x value increases. The WO_3 and $W_{19}O_{55}$ sensors show high response at temperature above 380 °C, while the W_5O_{14} and $W_{18}O_{49}$ sensors hold the best

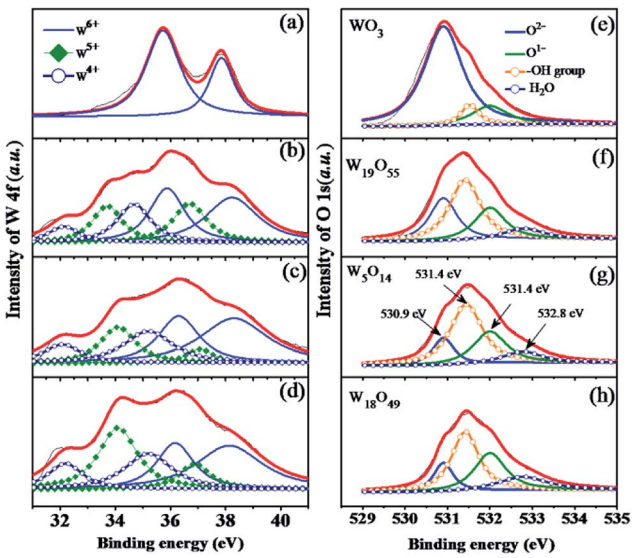

Fig. 3 (a–d) The W 4f-level and (e–h) O 1s-level XPS deconvolution spectra of the as-prepared sub-stoichiometric tungsten oxides, WO_3, $W_{19}O_{55}$, W_5O_{14}, and $W_{18}O_{49}$.

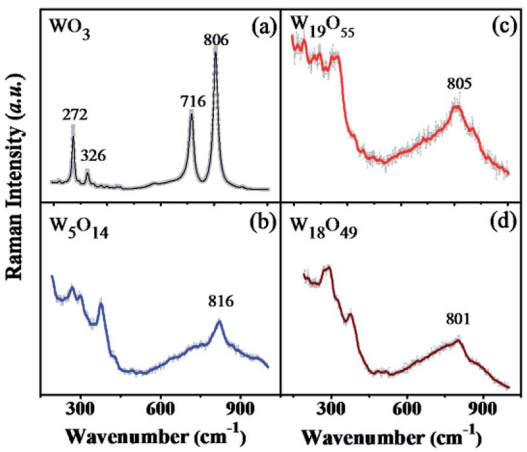

Fig. 4 The Raman spectra of the prepared sub-stoichiometric tungsten oxides, WO_3 (a), $W_{19}O_{55}$ (b), W_5O_{14} (c), and $W_{18}O_{49}$ (d).

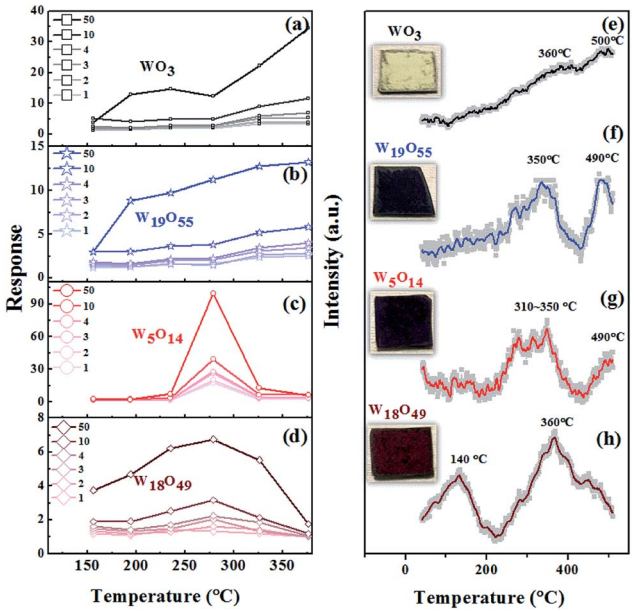

Fig. 5 (a–d) Temperature-dependent response curves of the gas sensors based on WO_3, sub-stoichiometric $W_{19}O_{55}$, W_5O_{14}, and $W_{18}O_{49}$ when exposed to different concentrations of H_2S (1, 2, 3, 4, 10, 50 ppm, marked in different shades of colour). (e–h) The O_2-TPD profiles for the four sensors and their corresponding photographs presented next to the curves.

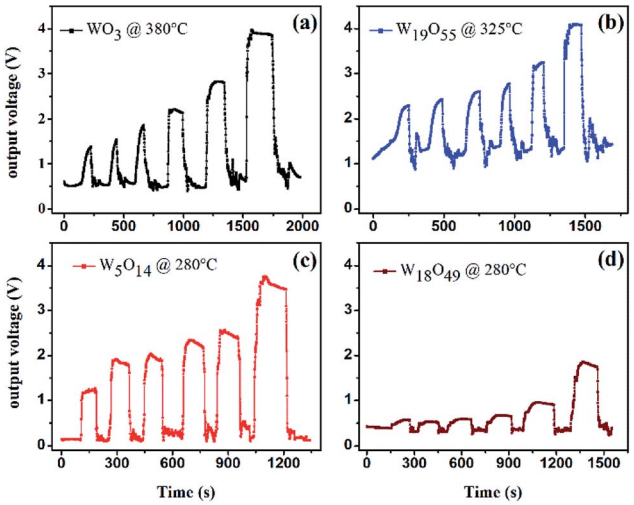

Fig. 6 Dynamic response curves of the sub-stoichiometric WO_{3-x} sensors: (a) WO_3 at 380 °C, (b) $W_{19}O_{55}$ at 325 °C, (c) W_5O_{14} and (d) $W_{18}O_{49}$ at 280 °C after exposed to 1, 2, 3, 4, 10, 50 ppm H_2S.

performance approximately at 280 °C. The $W_{18}O_{49}$ sensor presents a broad band sensitivity curve with a broad shoulder extending to the low temperature side ranging from 150 to 250 °C approximately. $W_{18}O_{49}$ has the highest density of oxygen vacancies among the tested sensors, suggesting that low-temperature sensing performance could be improved as a result of increasing concentration of oxygen vacancies. Thus, oxygen deficiency facilitates chemisorption of oxygen molecules on the WO_{3-x} surface. The W_5O_{14} sensor has a narrow temperature-dependent response curve with its highest response at around 280 °C. As a general trend, it is found that increasing oxygen vacancies give rise to enhanced device performance at low temperature as shown in Fig. 5(a–d), which is beneficial for applications.

To understand the oxygen absorption behaviours of the sub-stoichiometric tungsten oxide sensors, Fig. 5(e–h) display the temperature programmed desorption (O_2-TPD) profiles of the WO_{3-x} sensors, together with their photographs presented next to their corresponding curves. As the temperature increases, ambient oxygen molecules that are adsorbed on the tungsten-oxide surfaces undergo changes following the sequence of $O_2 \rightarrow O_2^- \rightarrow O^- \rightarrow O^{2-}$.[2] Physically adsorbed oxygen molecules (O_2) make ignorable contribution to gas sensing. The peaks of chemisorbed oxygen species (O_2^-, O^-, O^{2-}) are reported to centre around 400, 600 and >700 °C on the TPD curves.[33] Thus, Fig. 5(e) shows that the pristine WO_3 exhibits a broad desorption bands around 360 and 500 °C, attributed to the chemisorption of oxygen species O_2^- and O^-. For the $W_{19}O_{55}$ sensor, the two peaks are shifted to lower temperature positions at ~350 and ~490, as shown in Fig. 5(f). In the case of W_5O_{14}, strong peaks are observed at 310–350 °C (see Fig. 5(g)), while the peak at ~490 °C is rather weak. This indicates that a large amount of oxygen ions are chemisorbed in 310–350 °C, which might explain why there is a relatively strong response peak at ~280 °C, close to 310–350 °C where there are a lot of chemisorbed oxygen ions. As x increases to 0.28 ($W_{18}O_{49}$), a strong peak occurs at the low temperature of 140 °C shown by Fig. 5(h). The peak at 350 or 360 °C remains essentially unchanged. These results indicate that oxygen deficiency enhances chemisorption of oxygen ions on WO_{3-x} surface at low temperature by offering a large number of chemically active absorption sites, which in turn facilitates the ionosorption process and improves the low-temperature gas sensing sensitivity.[34–36] Thus, both the temperature-dependent response curves and the O_2-TPD profiles measured on the sub-stoichiometric WO_{3-x} sensors evidence that the working temperature of the gas sensors can be lowered down by using sub-stoichiometric nano WO_{3-x}.

The W_5O_{14} sensor presents the best performance over the narrow temperature range around 280 °C. However, $W_{18}O_{49}$ possesses the highest concentration of oxygen vacancies among all the sub-stoichiometric WO_{3-x} ones studied here, and the $W_{18}O_{49}$ sensor presents considerable response at low temperature. Obviously, the x value and the sensing sensitivity of the WO_{3-x} sensor do not have a simple relationship. Some other factors might affect device performance, such as specific surface area, crystallographic planes on the surface, and density of interfacial states, according to the published works.[18,37] Qin's work suggests that agglomeration of $W_{18}O_{49}$ at a comparatively high operating temperature weakens the gas diffusion, which in turn gives rise to low response.[34] Overall speaking, $W_{18}O_{49}$ is a metal-like material with abnormally high carrier concentration.[19,38] It is expected that the carrier concentration in $W_{18}O_{49}$ is comparable to the change of electron population induced by the target gas molecules. This leads to a relatively small resistance change when the sensor is exposed to the target gas,

compared to the result measured on the W_5O_{14} sensor. The $W_{18}O_{49}$ sensor, with the highest concentration of oxygen vacancies, thus possesses relatively low sensing response compared to the W_5O_{14} sensor, though its low-temperature performance is quite good.

The response and recovery times of the sensors are also investigated. Fig. 6(a–d) presents the dynamic response curves of the WO_3, $W_{19}O_{55}$, W_5O_{14}, and $W_{18}O_{49}$ sensors measured by the HW-30A gas sensing test system at given temperatures. The measured response (recovery) times are 67 s (65 s), 53 s (37 s), 21 s (11 s), and 32 s (15 s) for the WO_3, $W_{19}O_{55}$, W_5O_{14}, and $W_{18}O_{49}$ sensors, respectively. This overall results show the tendency that the use of sub-stoichiometric tungsten oxides accelerates response–recovery processes.

Conclusions

We have demonstrated that oxygen deficiencies facilitate the low-temperature oxygen ionosorption process, leading to the improvement of sensing performance of the WO_{3-x}-based gas sensors. High-quality sub-stoichiometric WO_{3-x} with several x values (WO_3, $W_{19}O_{55}$, W_5O_{14}, and $W_{18}O_{49}$) was synthesized and H_2S gas sensors were fabricated using the materials. The $W_{18}O_{49}$ sensor shows good device performance in a wide temperature range, particularly at the temperature as low as 150 °C. The W_5O_{14} gas sensor presents very high response value in a narrow temperature range centred at 280 °C. Our work shows that the sub-stoichiometric WO_{3-x} can be used to enhance the low temperature sensing performance through controlling the concentration of oxygen vacancies.

Conflicts of interest

There are no conflicts to declare.

Acknowledgements

This work is financially supported by National Key R&D Program of China (2016YFA0202200), National Natural Science Foundation of China (Grant no. 11574335, 61471345, 51772213), the Frontier Science Research Project (Key Programs) of Chinese Academy of Sciences (Grant no. QYZDJ-SSW-SLH018).

References

1 A. Gurlo and R. Riedel, *Angew. Chem., Int. Ed.*, 2007, **46**, 3826–3848.
2 A. Gurlo, *ChemPhysChem*, 2006, **7**, 2041–2052.
3 N. H. Al-Hardan, M. J. Abdullah, A. Abdul Aziz, H. Ahmad and L. Y. Low, *Vacuum*, 2010, **85**, 101–106.
4 S. W. Choi, J. Y. Park and S. S. Kim, *Nanotechnology*, 2009, **20**, 465603.
5 X. Song, Z. Wang, Y. Liu, C. Wang and L. Li, *Nanotechnology*, 2009, **20**, 075501.
6 H. G. Moon, Y. S. Shim, D. H. Kim, H. Y. Jeong, M. Jeong, J. Y. Jung, S. M. Han, J. K. Kim, J. S. Kim, H. H. Park, J. H. Lee, H. L. Tuller, S. J. Yoon and H. W. Jang, *Sci. Rep.*, 2012, **2**, 588.
7 D. Zhang, Z. Liu, C. Li, T. Tang, X. Liu, S. Han, B. Lei and C. Zhou, *Nano Lett.*, 2004, **4**, 1919–1924.
8 Y. Zhou, G. Xie, T. Xie, H. Yuan, H. Tai, Y. Jiang and Z. Chen, *Appl. Phys. Lett.*, 2014, **105**, 033502.
9 J. D. Fowler, M. J. Allen, V. C. Tung, Y. Yang, R. B. Kaner and B. H. Weiller, *ACS Nano*, 2009, **3**, 301–306.
10 L. Xu, R. Xing, J. Song, W. Xu and H. Song, *J. Mater. Chem. C*, 2013, **1**, 2174.
11 Z. Meng, H. Jian Xing and O. Chung Wo, *Nanotechnology*, 2012, **23**, 315503.
12 D. Jung, M. Han and G. S. Lee, *ACS Appl. Mater. Interfaces*, 2015, **7**, 3050–3057.
13 D. Jung, M. Han and G. S. Lee, *Sens. Actuators, A*, 2014, **211**, 51–54.
14 D. B. Migas, V. L. Shaposhnikov and V. E. Borisenko, *J. Appl. Phys.*, 2010, **108**, 093714.
15 F. Wang, C. Di Valentin and G. Pacchioni, *Phys. Rev. B*, 2011, **84**, 073103.
16 J. Song, Z.-F. Huang, L. Pan, J.-J. Zou, X. Zhang and L. Wang, *ACS Catal.*, 2015, **5**, 6594–6599.
17 Y. Qin, D. Hua and M. Liu, *J. Alloys Compd.*, 2014, **587**, 227–233.
18 Y. Qin, W. Xie, Y. Liu and Z. Ye, *Sens. Actuators, B*, 2016, **223**, 487–495.
19 S. Cong, F. Geng and Z. Zhao, *Adv. Mater.*, 2016, **28**, 10518–10528.
20 G. Xi, S. Ouyang, P. Li, J. Ye, Q. Ma, N. Su, H. Bai and C. Wang, *Angew. Chem.*, 2012, **124**, 2445–2449.
21 Y. Li, Y. Bando and D. Golberg, *Adv. Mater.*, 2003, **15**, 1294–1296.
22 W. Yu, Y. Sun, T. Zhang, K. Zhang, S. Wang, X. Chen and N. Dai, *Part. Part. Syst. Charact.*, 2016, **33**, 15–20.
23 J. Qian, Z. Peng, Z. Shen, Z. Zhao, G. Zhang and X. Fu, *Sci. Rep.*, 2016, **6**, 25574.
24 M. Remškar, J. Kovac, M. Viršek, M. Mrak, A. Jesih and A. Seabaugh, *Adv. Funct. Mater.*, 2007, **17**, 1974–1978.
25 Z. Shen, Z. Zhao, J. Wen, J. Qian, Z. Peng and X. Fu, *J. Nanomater.*, 2018, **2018**, 1–12.
26 Z. Shen, Z. Zhao, J. Qian, Z. Peng and X. Fu, *J. Mater. Res.*, 2016, **31**, 1065–1076.
27 C.-Y. Su, H.-C. Lin, T.-K. Yang, C.-H. Chang and C.-K. Lin, *Mater. Trans.*, 2009, **50**, 2593–2597.
28 J. Qian, Z. Zhao, Z. Shen, G. Zhang, Z. Peng and X. Fu, *RSC Adv.*, 2016, **6**, 8061–8069.
29 K. Thummavichai, L. Trimby, N. Wang, C. D. Wright, Y. Xia and Y. Zhu, *J. Phys. Chem. C*, 2017, **121**, 20498–20506.
30 J. C. Dupin, D. Gonbeau, P. Vinatier and A. Levasseur, *Phys. Chem. Chem. Phys.*, 2000, **2**(6), 1319–1324.
31 A. Shpak, M. Korduban, M. M. Medvedskij and V. O. Kandyba, *J. Electron Spectrosc. Relat. Phenom.*, 2007, **156–158**, 172–175.
32 C. Jian, L. Dongyu, Z. Weihong, X. Fangyan, Z. Jun, G. Li, L. Xiao, D. Shaozhi and X. Ningsheng, *J. Phys. D: Appl. Phys.*, 2008, **41**, 115305.

33 X. Huang, Y. Peng, X. Liu, K. Li, Y. Deng and J. Li, *Catal. Commun.*, 2015, **69**, 161–164.
34 Y. Qin, M. Hu and J. Zhang, *Sens. Actuators, B*, 2010, **150**, 339–345.
35 J. Liu, Y. Gao, X. Wu, G. Jin, Z. Zhai and H. Liu, *Sensors*, 2017, **17**, 1852.
36 J. Wu, Q. Huang, D. Zeng, S. Zhang, L. Yang, D. Xia, Z. Xiong and C. Xie, *Sens. Actuators, B*, 2014, **198**, 62–69.
37 C. T. Pan, C. Y. Su and Y. C. Luo, *Microsyst. Technol.*, 2016, **23**, 2113–2123.
38 E. Salje and B. Güttler, *Philos. Mag. B*, 1984, **50**, 607–620.